Supporting Information

Crystal Structures, CO_2 Adsorption, and Dielectric Properties of $[Cu(II)_2(R\text{-Benzoate})_4(\text{pyrazine})]_\infty$ Polymers (R = m-F, 2, 3-F_2, m-Cl, and m-CH_3)

Kiyonori Takahashi,[†] *Norihisa Hoshino,*[†, ‡] *Takashi Takeda,*[†, ‡] *Shin-ichiro Noro,*[¶] *Takayoshi Nakamura,*[¶] *Sadamu Takeda,*[±] *Tomoyuki Akutagawa*[†, ‡*]

Infrared spectroscopy

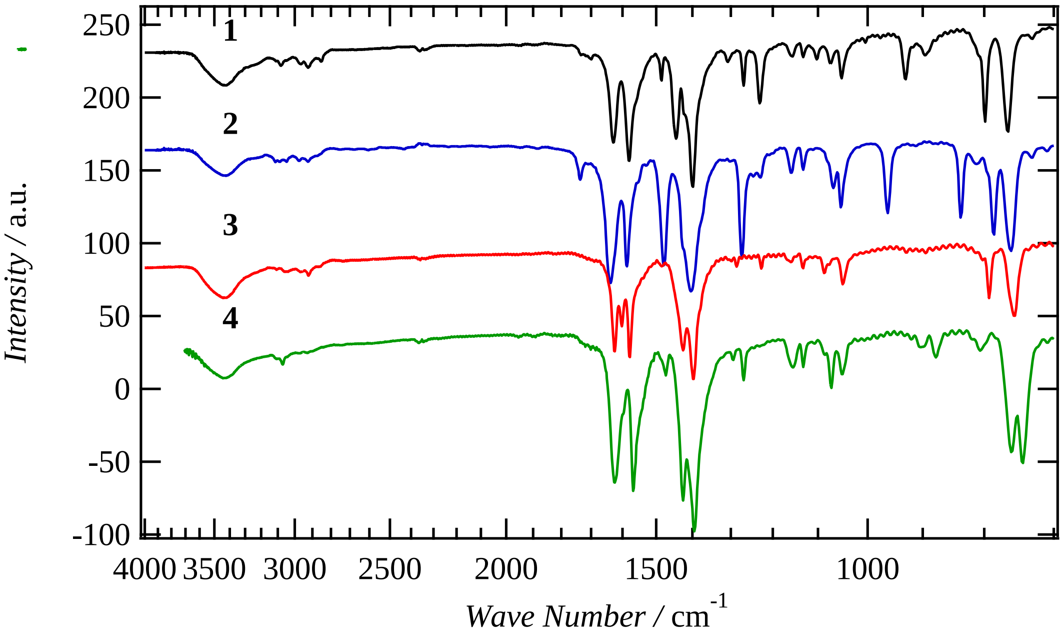

Figure S1. Infrared Spectra of **1** ~ **4**, ranged from 700 to 4000 cm^{-1}. Black, blue, red and green colored lines correspond with **1**, **2**, **3** and **4**, respectively. All complexes had the broad peak from 3200 ~ 3600 cm^{-1}, and these spectra were come from O-H stretching of H_2O. So these results indicated that after the crystals were picked up from the solvent to the ambient condition, all complexes absorbed H_2O.

Uv-vis spctroscopy

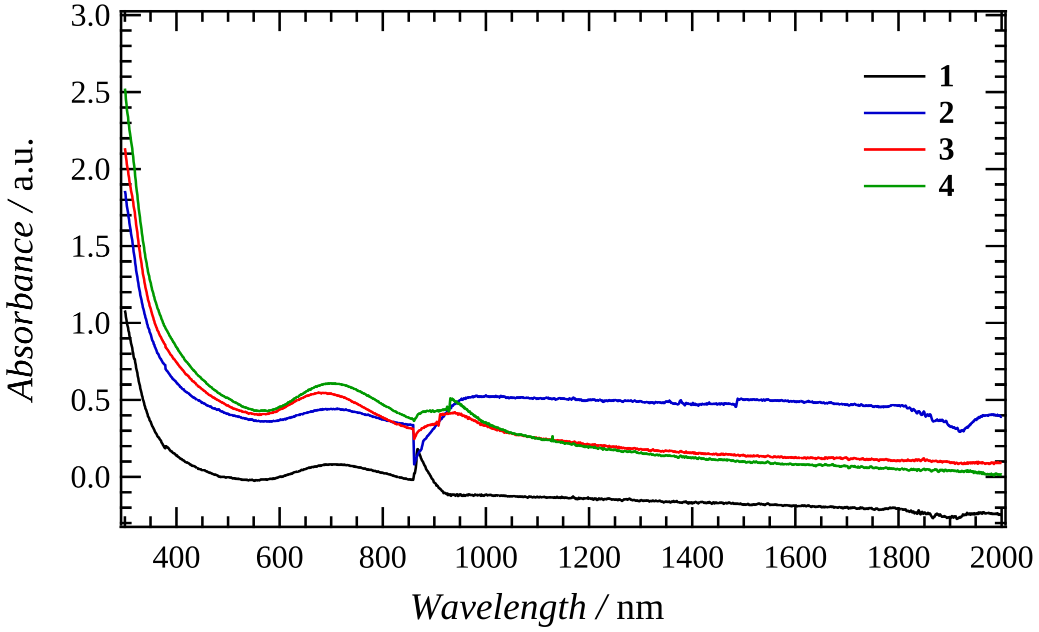

Figure S2. UV-vis spectra of **1** ~ **4**, ranged from 300 to 2000 cm^{-1}. Black, blue, red and green colored lines correspond with **1**, **2**, **3** and **4**, respectively.

Variable Temperature X-ray Diffraction

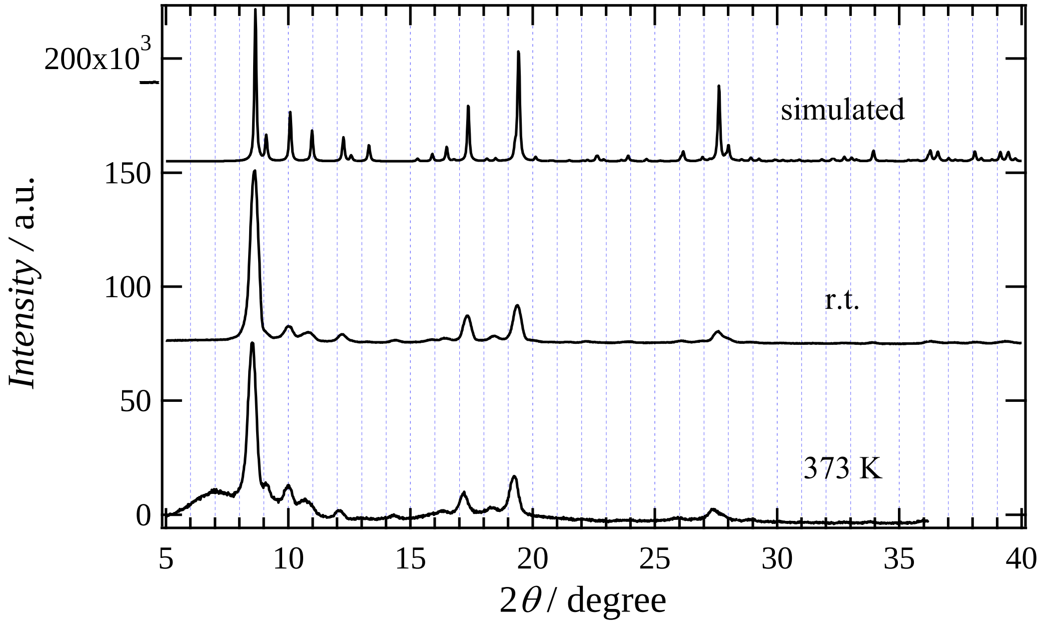

Figure S3. The variable temperature powder X-ray diffraction patterns for **1**. The second and third patterns from the top were measured at room temperature and 373 K. The first pattern from the top was simulated from the single crystal structure of **1**·$4CH_3CN$.

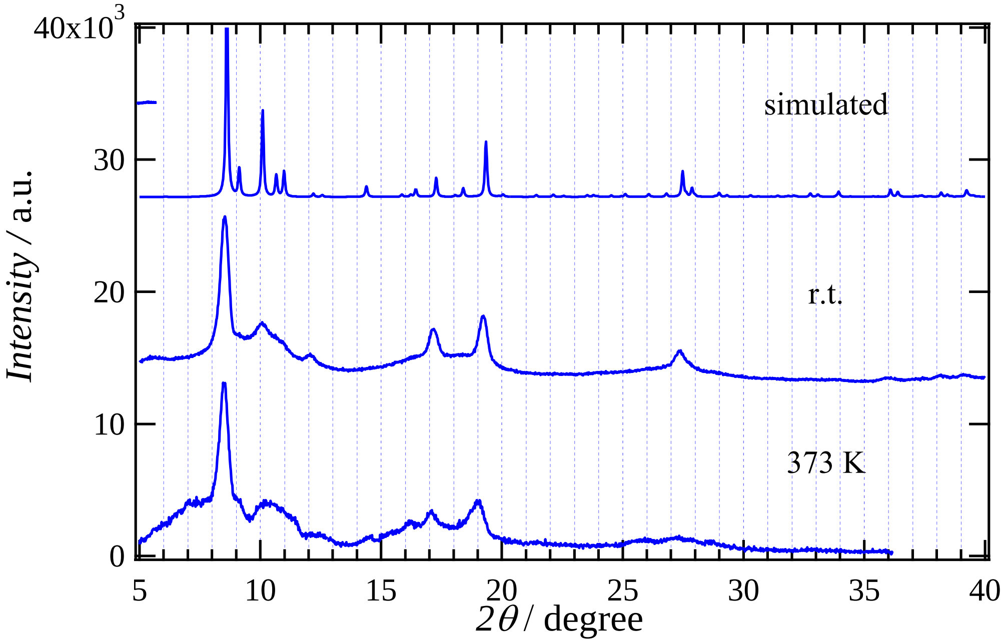

Figure S4. The variable temperature powder X-ray diffraction patterns for **2**. The second and third patterns from the top were measured at room temperature and 373 K. The first pattern from the top was simulated from the single crystal structure of **2**·4CH_3CN.

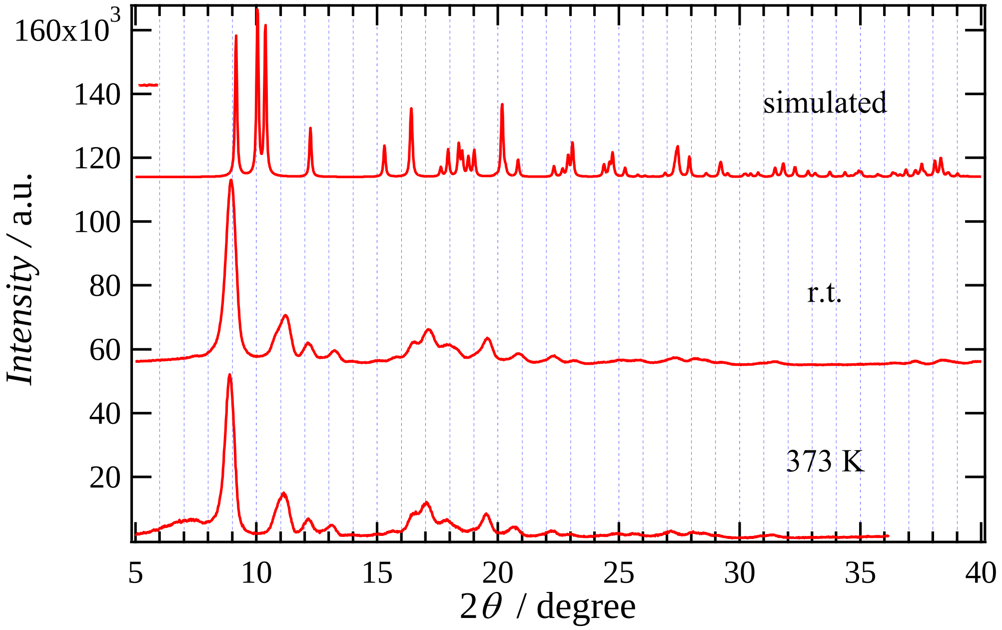

Figure S5. The variable temperature powder X-ray diffraction patterns for **3**. The second and third patterns from the top were measured at room temperature and 373 K. The first pattern from the top was simulated from the single crystal structure of **3**·2CH_3CN.

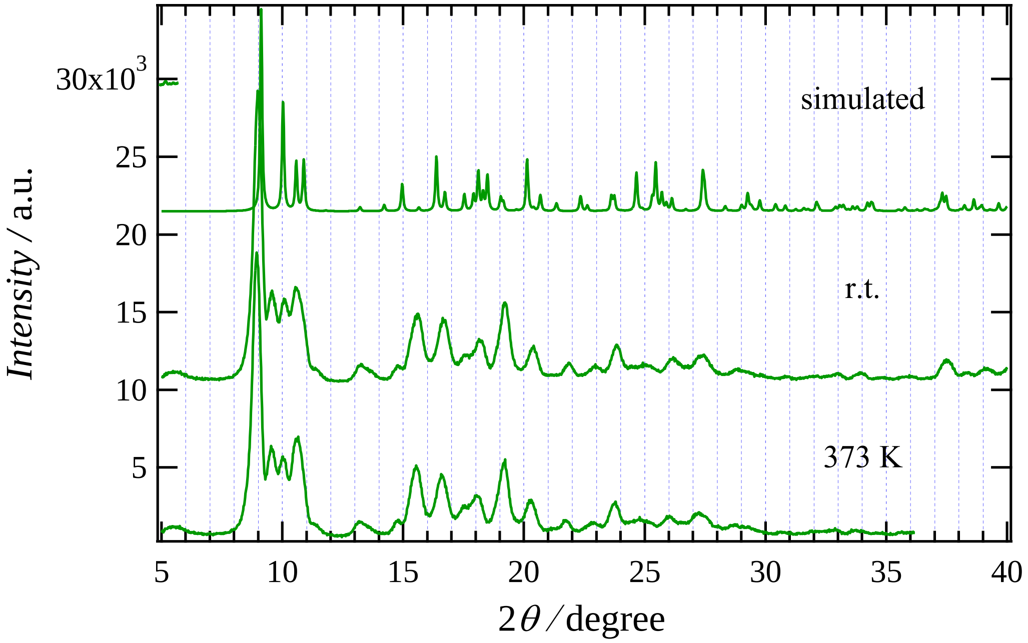

Figure S6. The variable temperature powder X-ray diffraction patterns for **4**. The second and third patterns from the top were measured at room temperature and 373 K. The first pattern from the top was simulated from the single crystal structure of **4**·2CH_3CN.

The variable temperature X-ray diffraction patterns of **1** ~ **4** were summarized in the Figures S3 ~ S6. The patterns of **1** and **2** indicated the two results: the crystal structures of **1** and **2** are stable to the change in the temperature to 373 K, and the structures are not changed by the replacement of the crystallized solvent CH_3CN. The patterns of **3** and **4** (Figures S5, and S6) indicated that the crystal structure of **3** and **4** are stable to the changes in the temperature to 373 K, but by comparison with simulated patterns, the structures are changed by the replacement of the crystallized solvent CH_3CN.

Crystal Structures

Independent structures and coordination geometries.

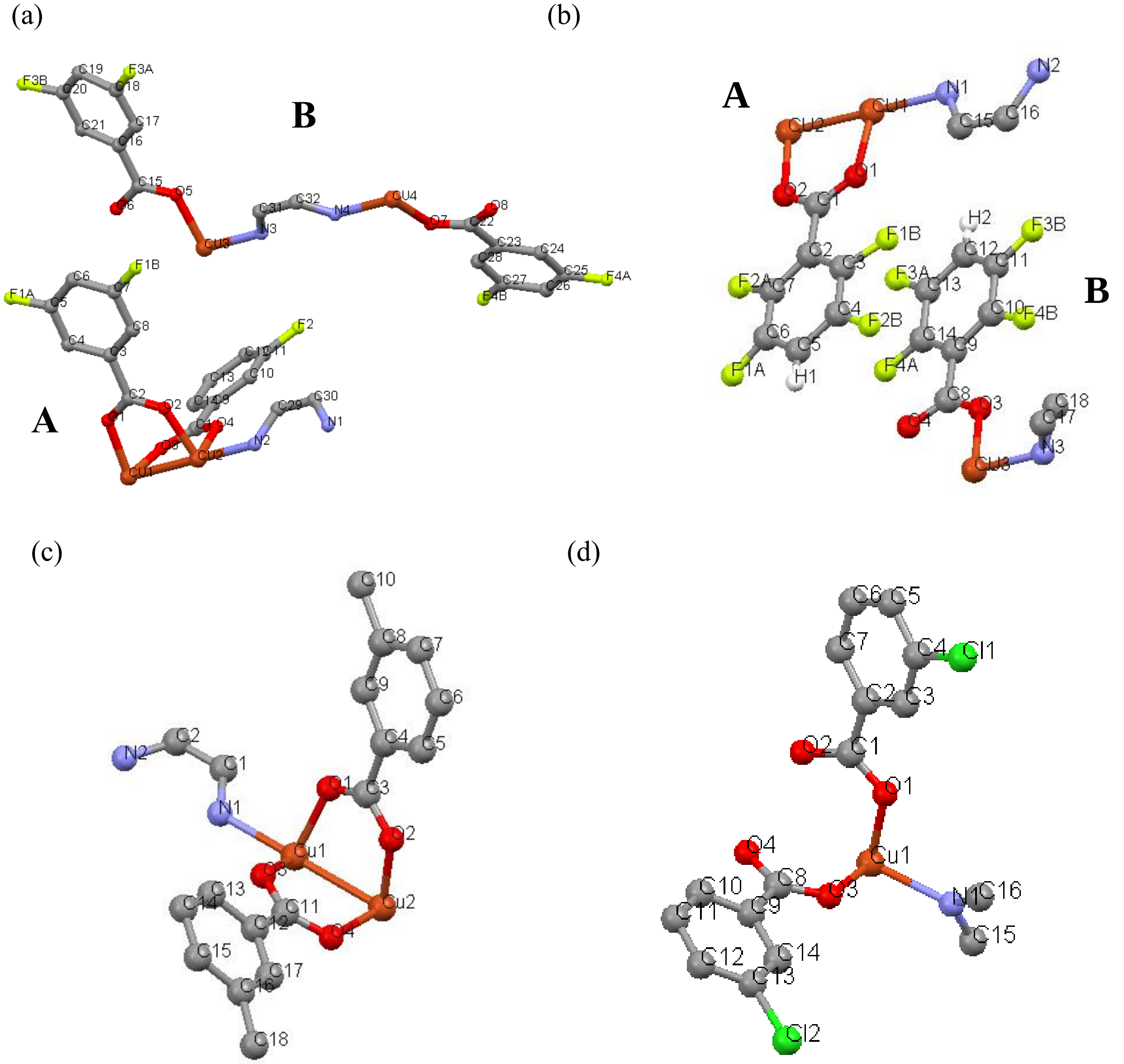

Figure S7. Independent molecular structures. Hydrogen atoms and crystallization solovents are omitted for clarity. By the symmetrical operation, paddle-wheel type structures were constructed. (a) Crystal **1**•4CH$_3$CN had two independent molecular structures shown as **A** and **B** unit, and the each unit had the same molecular formula Cu$_2$C$_{16}$H$_{10}$N$_2$O$_4$F$_2$. (b) Crystal **2**•4CH$_3$CN had also two independent molecular structures shown as **A** and **B** unit, but the each unit had the different molecular formula; formula of **A**-unit was C$_9$H$_5$N$_2$O$_2$F$_2$Cu$_2$, and formula of **B**-unit was C$_1$H$_5$N$_1$O$_2$F$_2$Cu$_1$. (c) Crystal

3•2CH$_3$CN had one independent unit and its formula was $C_{18}H_{16}N_2O_4Cu_2$. (d) Crystal **4**•2CH$_3$CN also had one independent unit and its formula was $C_{16}H_{10}N_2O_4ClCu_2$.

Table S1. Selected structural distance of crystals **1** - **4**.

Crystal	**1**•4CH$_3$CN	**2**•4CH$_3$CN	**3**•2CH$_3$CN	**4**•2CH$_3$CN
$d_{Cu\sim Cu}$, Å [a]	2.604	2.599	2.582	2.624
$d'_{Cu\sim Cu}$, Å [a]	7.082	7.069	7.157	7.113
$d_{Cu\sim O}$, Å [b]	1.968	1.962	1.970	1.961
$d_{Cu\sim N}$, Å [c]	2.152	2.14	2.178	2.181

[a] The $d_{Cu\sim Cu}$ was the Cu~Cu distance in the paddle-wheel unit, whereas the $d'_{Cu\sim Cu}$ was the Cu~Cu distance between the paddle-wheel unit through the pz ligand. [b] The $d_{Cu\sim O}$ was the average Cu~O distance in the paddle-wheel unit. [c] The $d_{Cu\sim N}$ was the average Cu~N distance in the axially coordinated pz ligand.

The average Cu-Cu distances ($d_{Cu\sim Cu}$) in the dimer units of polymers **1**, **2**, **3**, and **4** were $d_{Cu\sim Cu}$ = 2.604, 2.599, 2.582, and 2.624 Å, respectively, whereas the average Cu-Cu distances ($d'_{Cu\sim Cu}$) between the binuclear units through the pz ligand ranged from $d'_{Cu\sim Cu}$ = 7.069 to 7.157 Å (Table 2). The average Cu~O distances ($d_{Cu\sim O}$) in polymers **1**-**4** were in the range from 1.961 to 1.970 Å, which supports the same Cu(II) coordination environment. The dihedral angle of two neighboring *R*-BA ligands (ϕ_1) in the paddle-wheel unit was slightly different to each other. The magnitude of ϕ_1 was decreased in the order of **2** (ϕ_1 = 90 °), **1** (ϕ_1 = 86.8 °), **4** (ϕ_1 = 83.05 °), and **3** (ϕ_1 = 77.21 °). The introduction of relatively large size Cl- and CH$_3$-groups into the *m*-position of BA ligand decreased the dihedral angle of ϕ_1 in contrast with those of crystals **1** and **2**. The parallel arrangement of pz ligands in polymers **3** and **4** was observed along the *c* axis. The dihedral angles between the π-planes of two neighboring pz lignads in the **A**- and **B**-chains in crystal **1** were 45 and 90 °, respectively. The pz orientation in **A**-chain of crystal **2** was not determined due to orientational disorders, whereas the orthogonal arrangement of pz-ligands was observed in **B**-chain.

Tables S2 ~ S10 summarized the bond distances and bond angles around Coppers and the bridging ligands in the crystal **1**•4CH_3CN ~ **4**•2CH_3CN. The number for atoms in the tables corresponds to those of Figures S7. These tables indicated that all coppers had octahedral coordinated geometry. All angles and distances of the bridging ligands were very similar to each other, so electrons on the bridging ligands were delocalized.

Aside from the orientation of the substituent group at the *m*-position of the BA ligand, the molecular structures of the Cu(II) binuclear unit in polymers **1**-**4** were the same. The dihedral angles of two neighboring *R*-BA ligands (ϕ_1) in the paddle-wheel unit were slightly different. The magnitude of ϕ_1 was decreased in the order of **2** (ϕ_1 = 90°), **1** (ϕ_1 = 86.8°), **4** (ϕ_1 = 83.05°), and **3** (ϕ_1 = 77.21°). The introduction of relatively large size Cl- and CH_3-groups into the *m*-position of the BA ligand decreased ϕ_1 in contrast with those of crystals **1** and **2**. A parallel arrangement of the pz ligands in polymers **3** and **4** was observed along the *c* axis. The dihedral angles between the π-planes of two neighboring pz ligands in the **A**- and **B**-chains of crystal **1** were 45 and 90°, respectively.

Table S2. The distances around Coppers of Crystal **1**•4CH_3CN.

bond lengths	
A	
Cu1-Cu2	2.6020(10)
Cu1-O1	1.954(3)
Cu1-O3	2.002(3)
Cu1-N1a	2.185(4)
Cu2-O2	1.973(3)
Cu2-O4	1.954(3)
Cu2-N2	2.142(4)
B	
Cu3-Cu3a	2.6044(19)
Cu3-O5	1.949(3)
Cu3-O6a	1.981(3)
Cu3-N3	2.145(5)
Cu4-Cu4a	2.6084(18)
Cu4-O7	1.948(3)
Cu4-O8a	1.986(3)
Cu4-N4	2.171(5)

Table S3. Bond angles around Coppers of crystal **1**•4CH_3CN.

bond angles [°]	
A	
O1-Cu1-O3	89.74(15)
O1-Cu1-N1	93.74(9)
O3-Cu1-N1	97.45(10)
O2-Cu2-O4	88.8(1)
O2-Cu2-N2	96.94(9)
O4-Cu2-N2	93.36(10)
B	
O5-Cu3-O6	90.80(14)
O6-Cu3-N3	96.72(10)
O5-Cu3-N3	93.81(10)
O7-Cu4-O8	88.93(14)
O8-Cu4-N4	96.65(10)
O7-Cu4-N4	93.58(10)

Table S4. Bond angles and distances around briged parts of *m*-FBA of crystal **1**•4CH_3CN.

bond angles [°]	
A	
O3-C1-O4	124.3(5)
O1-C2-O2	125.5(4)
B	
O5-C15-O6	125.4(5)
O7-C22-O8	126.0(5)

bond length [Å]	
A	
C1-O3	1.251(5)
C1-O4	1.286(5)
C2-O1	1.283(6)
C2-O2	1.246(6)
B	
C15-O5	1.252(6)
C15-O6	1.272(5)
C22-O7	1.255(5)
C22-O8	1.278(5)

Table S5. The distances and bond angles around Coppers of Crystal **2**•4CH_3CN.

Distances [Å]	
A	
Cu1-Cu2	2.584(2)
Cu1-O1	1.967(4)
Cu1-N1	2.348(11)
Cu2-O2	1.971(4)
Cu2-N2	1.913(11)
B	
Cu3-Cu3a	2.602(2)
Cu3-O4	1.969(4)
Cu3-O3	1.984(4)
Cu3-N3	2.129(10)
bond Angles [°]	
A	
O1-Cu1-O1	89.6(2)
O2-Cu2-O2	89.6(2)
O1-Cu1-N1	94.6(3)
O2-Cu2-N2	94.7(3)
B	
O3-Cu3-O4	89.2(2)
O3-Cu3-N3	96.2(3)
O4-Cu3-N3	94.8(3)

Table S6. Bond angles and distances around briged parts of 2,3-F_2BA of crystal **2**•4CH_3CN.

bond angles [°]	
A	
O2-C1-O1	125.5(6)
B	
O3-C8-O4	126.6(6)

bond length [Å]	
A	
O1-C1	1.276(7)
O2-C1	1.275(7)
B	
O3-C8	1.241(7)
O4-C8	1.245(7)

Table S7. The distances and bond angles around Coppers of Crystal **3**•2CH_3CN.

distances [Å]	
Cu1-Cu2	2.5821(6)
Cu1-O1	1.987(1)
Cu1-O3	1.962(1)
Cu1-N1	2.178(4)
Cu2-O2	1.962(1)
Cu2-O4	1.968(1)
Cu2-N2	2.189(4)
Angles [°]	
O1-Cu1-O3	89.25(5)
O2-Cu2-O4	88.99(5)
O1-Cu1-N1	95.4(1)
O2-Cu2-N2	96.4(1)

Table S8. Bond angles and distances around briged parts of *m*-MBA of crystal **3**•2CH_3CN.

bond angles [°]	
O1-C3-O2	125.1(2)
O3-C11-O4	125.3(2)
bond length [Å]	
C3-O1	1.263(3)
C3-O2	1.268(3)
C11-O3	1.270(3)
C11-O4	1.262(3)

Table S9. The distances and bond angles around Coppers of Crystal **4**•2CH_3CN.

distances [Å]	
Cu1-Cu1a	2.6236(9)
Cu1-O1	1.971(4)
Cu1-O2	1.963(4)
Cu1-O3	1.955(3)
Cu1-O4	1.957(3)
Cu1-N4	2.181(4)
Angles [°]	
O1-Cu1-O3	90.2(1)
O1-Cu1-O4	90.6(2)
O2-Cu1-O3	87.9(2)
O2-Cu1-O4	89.2(2)
O1-Cu1-N1	96.7(2)
O2-Cu1-N1	94.3(2)
O3-Cu1-N1	97.0(1)
O4-Cu1-N1	94.0(2)

Table S10. Bond angles and distances around briged parts of *m*-MBA of crystal **4**•2CH_3CN**.**

bond angles [°]	
O1-C1-O2	125.6(5)
O3-C8-O4	125.0(5)
bond length [Å]	
C8-O3	1.261(7)
C8-O4	1.270(6)

1D Void Structure of **3**•2CH$_3$CN and **4**•2CH$_3$CN.

In this supporting information, 1D void Structure of **3**•2CH$_3$CN and **4**•2CH$_3$CN are described.

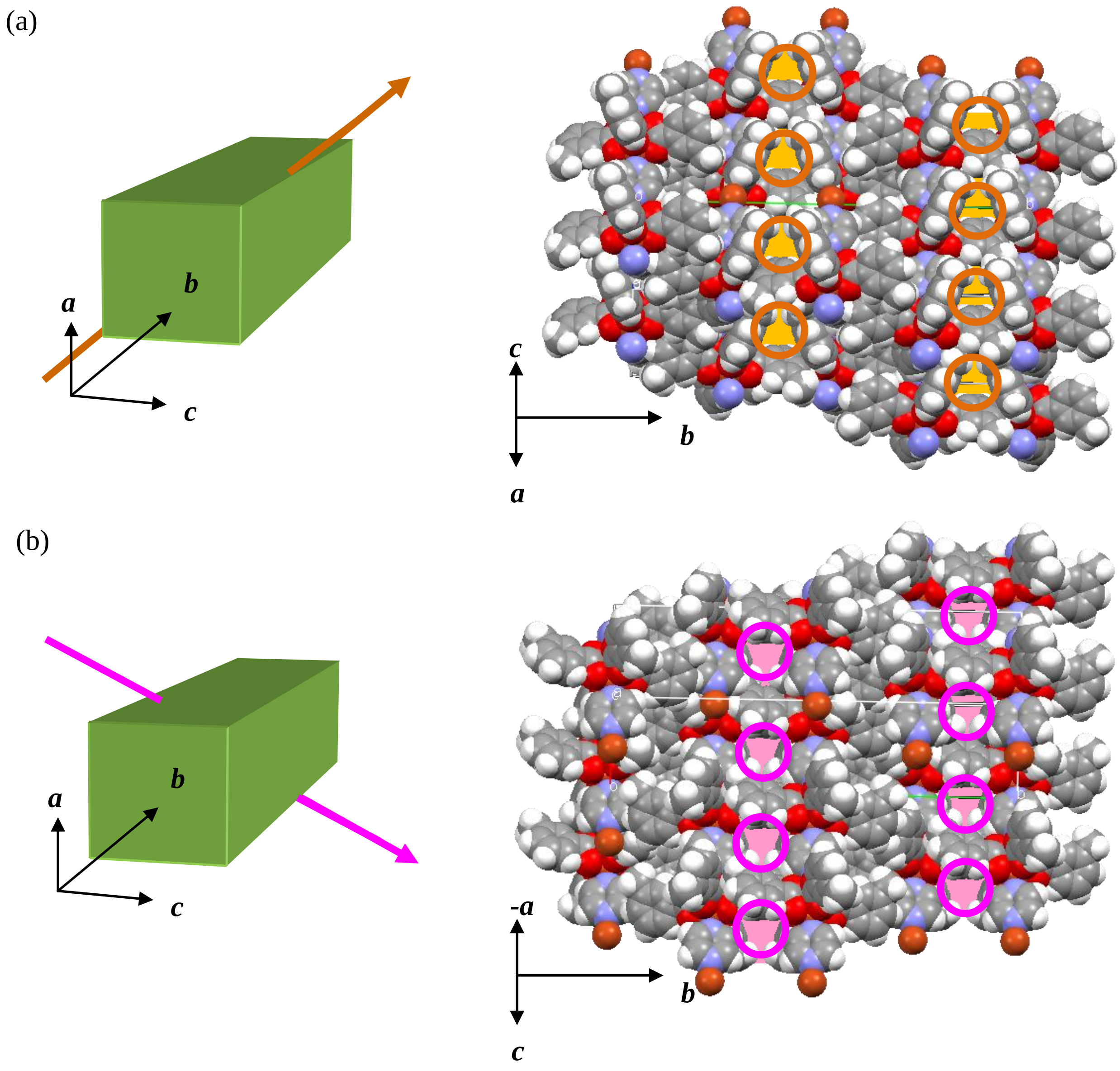

Figure S8. Two kinds of 1D channel Structures of crystal **3**•2CH$_3$CN. The Crystallization solvents are omitted for clarity. (a) Left: Model of Unit cell (green) and the orange colored line shows how to see unit cell on the right figure, Right: Unit cell shown as the space filling model viewed along with *a*+*c* axis. Orange colored markers mean 1D channel strucutures. (b) Left: Model of Unit cell (green) and the pink colored line shows how to see unit cell on the right figure, Right: Unit cell shown as the space filling model viewed along with -*a*+*c* axis. pink colored markers mean 1D channel strucutures.

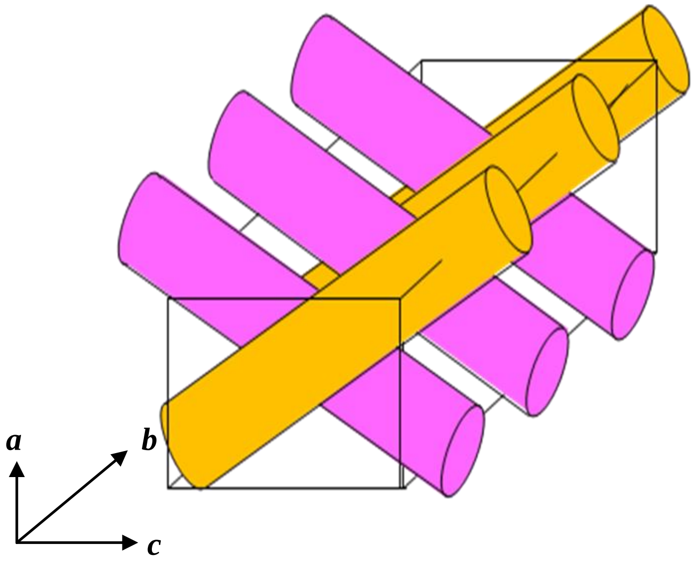

Figure S9. The model of arrangement of 1D channel structure. The orange and pink colors are correspond to the colors on Figure S8. 1D channel structures were alternatively arranged like *a*+*c* and -*a*+*c* directions in the crystal of **4**•2CH$_3$CN. In these channels, the crystallization solvents are arranged.

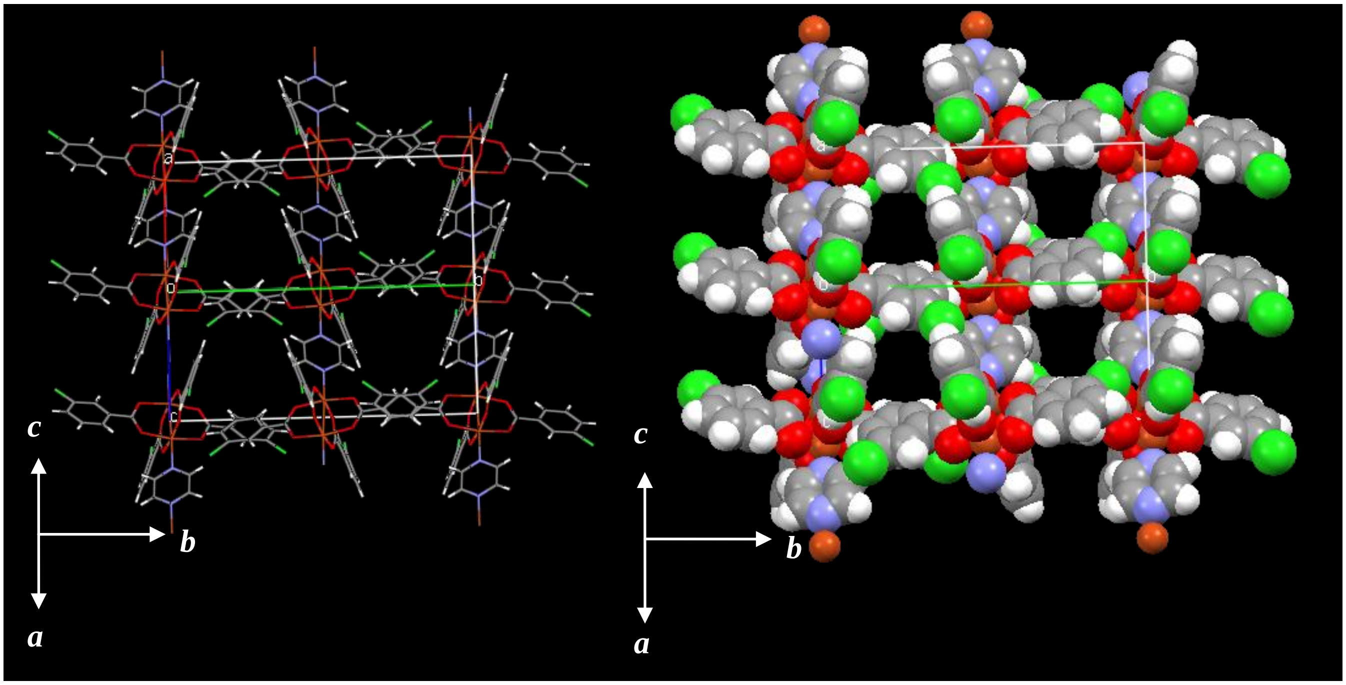

Figure S10. 1D channel Structure of crystal **4**•2CH$_3$CN viewed along *a*+*c* axis. The Crystallization solvents are omitted for clarity. Left: Wireframe model of the packing structure, Right: Space filling model of the packing structure.

Crystallized Solvents

Although calculation of the void volume (V_{void} = 161 Å^3) per [Cu(II)$_2$(*m*-FBA)$_4$(pz)] unit in crystal **1** is consistent with four CH_3CN molecules (4×CH_3CN ca. 40 Å^3 = ca. 160 Å^3) with the formula **1**•4CH_3CN, the crystal structural analysis indicated the formula **1**•3CH_3CN, where one CH_3CN molecule could not be observed in the residual electron densities due to the quality of the single crystal. Rapid weight loss in the TG profile suggests the possible removal of one CH_3CN molecule from **1**•4CH_3CN during the single crystal hand-picking procedure. The crystal formula of **2**•4CH_3CN for the as-grown crystal was rapidly changed to the desolvated crystal or hydrated **2**•3H_2O crystal under the ambient conditions. The magnitudes of the V_{void} for crystals **3** and **4** were 76 and 90 Å^3, respectively, which were consistent with two CH_3CN molecules (ca. 80 Å^3) in the channel.

Occupancy Factors

Crystal 1•4CH$_3$CN: The occupancy factors of disordered F-sites were different; F1A:F1B = 0.5:0.5, F3A:F3B = 0.7:0.3, and F4A:F4B = 0.8:0.2. In the **A**-chain, the fixed orientation of the F2-site and equal occupancy for the F1A:F1B = 0.5:0.5 pair generated a net dipole moment along the +*c* axis. In **B**-chain, the net dipole moment was cancelled by the alternate arrangement of F3A and F3B sites within the paddle-wheel unit. The same ligand arrangement of F4A and F4B sites within the paddle-wheel unit was observed in **B**-chain. It is difficult to discuss the parallel or antiparallel arrangements in crystal 1 with respect to the orientational disorder of the F-groups. From the occupancy factors of F1A:F1B = 0.5:0.5, F3A:F3B = 0.7:0.3, and F4A:F4B = 0.8:0.2, the antiparallel dipole arrangement of F-groups within the π-dimer should be the dominant intermolecular interaction.

Crystal 2•4CH$_3$CN: The occupancy factors for F1A:F1B and F3A:F3B should be same as those for F2A:F2B and F4A:F4B, respectively. The occupancy factors for F1A:F1B in the **A**-chain and F3A:F3B in the **B**-chain were determined to be 0.7:0.3 and 0.7:0.3, respectively. From the occupancy factors of F1A:F1B = F2A:F2B = F3A:F3B = F4A:F4B = 0.7:0.3, the outer F-groups in the π-dimer have larger occupancy factors than those of the inner groups, which suggests that the antiparallel outer orientation of the 2,3-F2BA ligand is the dominant interchain interaction of the π-dimer in crystal **2**. The pz orientation in the A-chain of crystal 2 was not determined due to orientational disorder, whereas an orthogonal arrangement of the pz-ligands was observed in the B-chain.

Crystal 3•2CH_3CN and 4•2CH_3CN: No orientational disorder of the *m*-MBA and *m*-ClBA ligands was observed (see Figures 2c and 2d).

Crystal shapes.

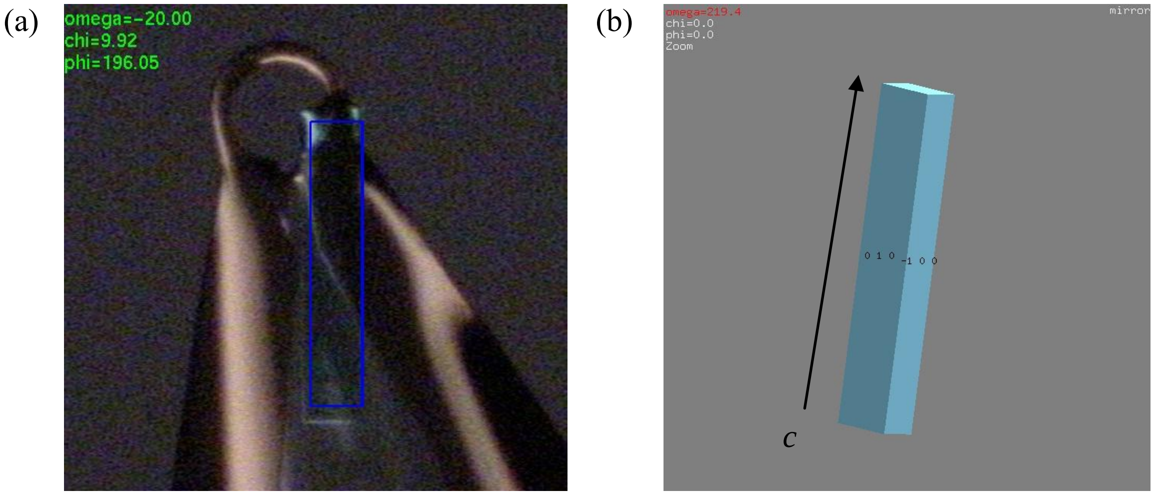

Figure S11. (a) Crystal shape of **1**•4CH_3CN mounted on thin polyimide films (MiTeGen MicroMounts). (b) Crystal shape calculated by Rigaku RAPID-II. The longest axis of the crystal shape corresponded to the chain direction, *c*-axis. Crystals **2**•4CH_3CN and **3**•2CH_3CN construct the same crystal shape with crystal **1**•4CH_3CN.

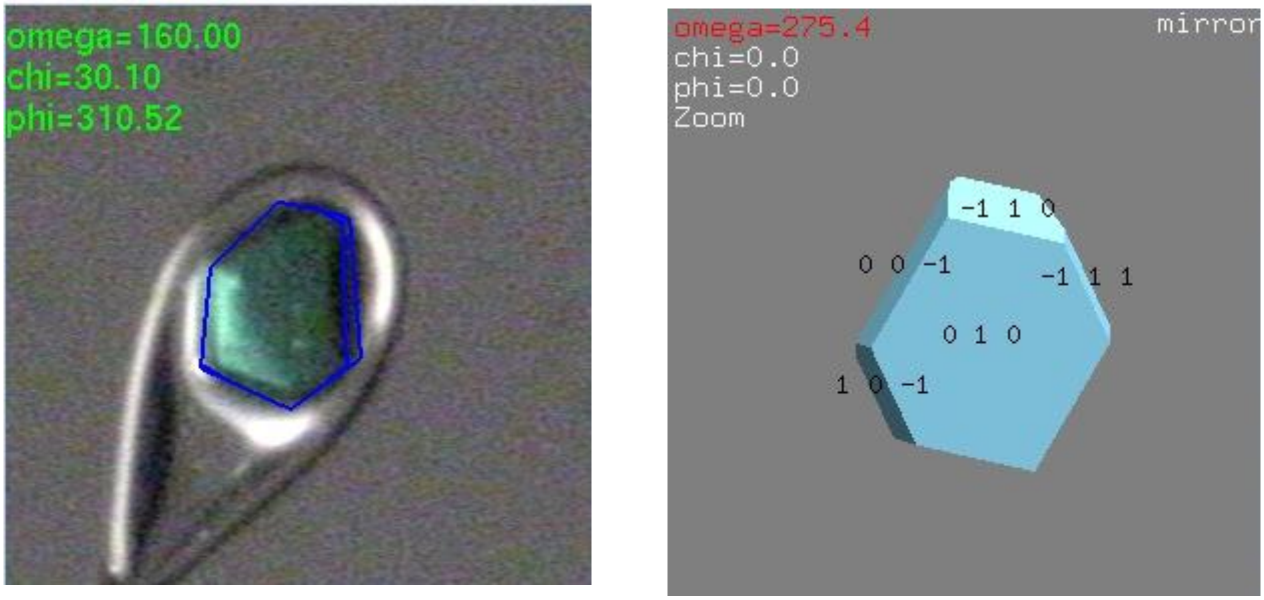

Figure S12. (a) Crystal shape of **4**•2CH_3CN mounted on thin polyimide films (MiTeGen MicroMounts). (b) Crystal shape calculated by Rigaku RAPID-II. The crystal shape of **4**•2CH_3CN was different from the others, and it shape is like platelet.

N_2 adsorption-desorption isotherms.

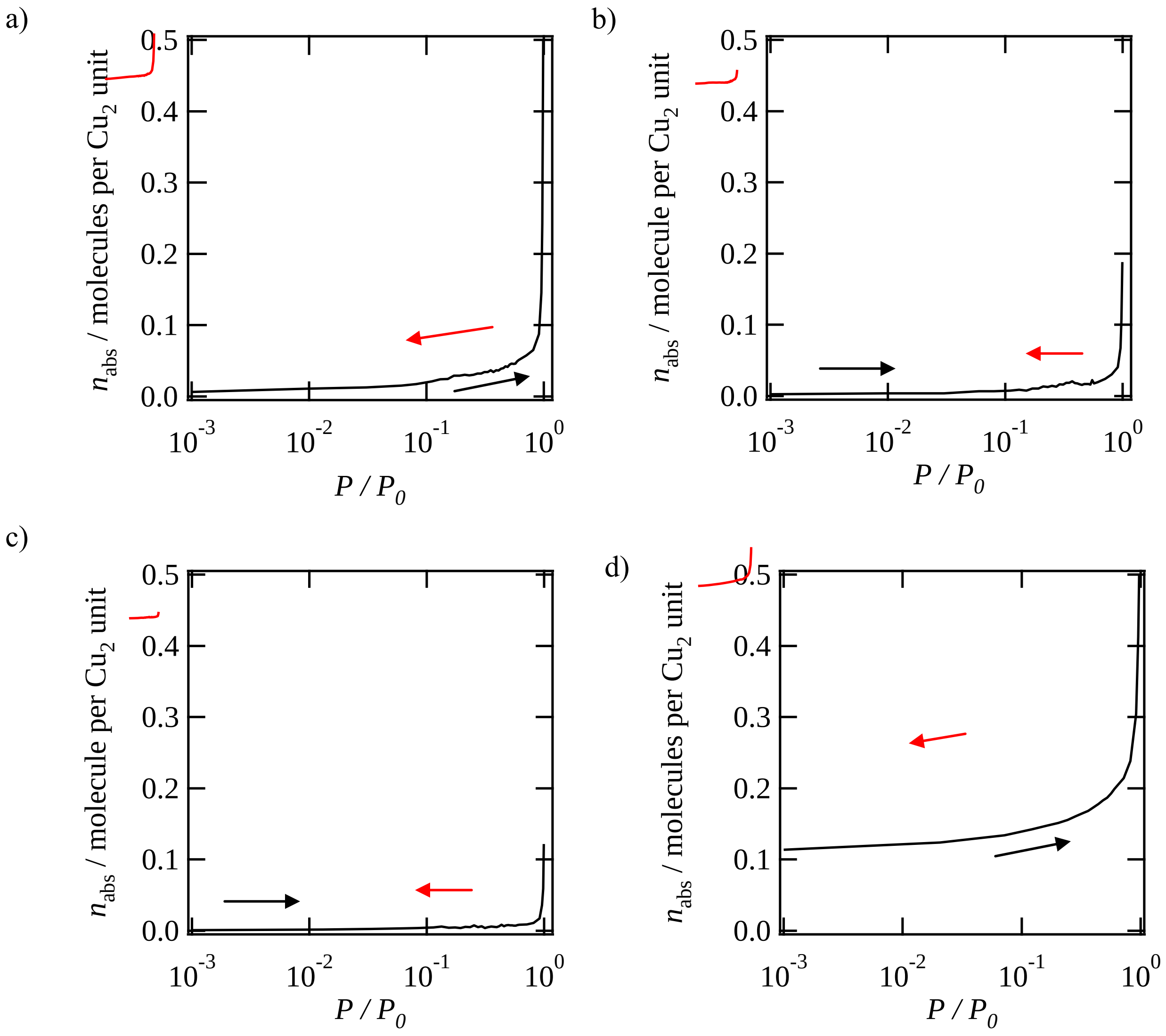

Figure S13. N_2 adsorption-desorption isotherms for crystals a) **1**, b) **2**, c) **3**, and d) **4** per $[Cu(II)_2(BA)_4{\cdot}(pz)]$ unit at 77 K. The black ($10^{-3} < P/P_0 < 10^{0}$) and red ($10^{0} > P/P_0 > 10^{-2}$) lines represent adsorption and desorption processes, respectively.

Temperature- and frequency-dependent dielectric constants of 3 and 4.

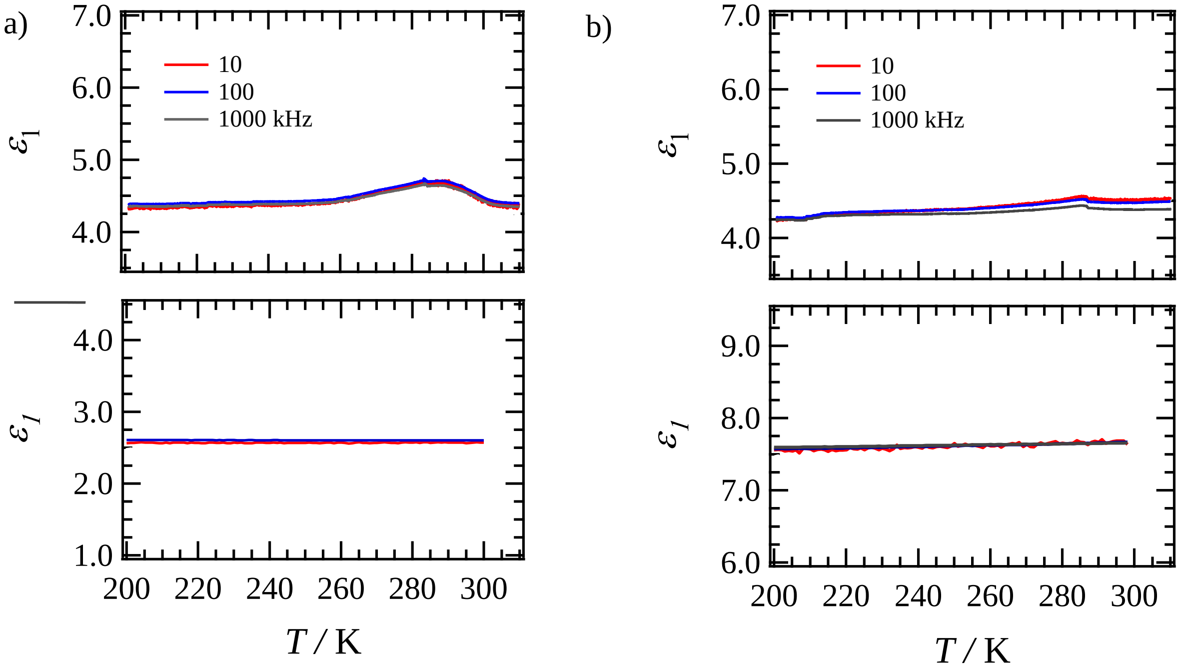

Figure S14. Temperature- ($200 < T < 310$ K) and frequency-dependent ($f = 10$, 100, and 1000 kHz) dielectric constants (ε_1) of crystals a) **3** and b) **4**. Pellet samples were used for measurements in vacuum (lower figure) and CO_2 adsorption condition (upper figure).